International Journal of Heat and Fluid Flow 30 (2009) 868–876

Contents lists available at ScienceDirect

International Journal of Heat and Fluid Flow

journal homepage: www.elsevier.com/locate/ijhff

# Gas–liquid flows in a microscale fractal-like branching flow network

Younghoon Kwak [b], Deborah Pence [a,*], James Liburdy [a], Vinod Narayanan [a]

[a] Oregon State University, School of Mechanical Industrial and Manufacturing Engineering, 204 Rogers Hall, Corvallis, OR 97331-6001, USA
[b] CAE Group, Corporate R&D Institute, Samsung Electro-Mechanics CO., Ltd., South Korea

ARTICLE INFO

*Article history:*
Received 29 November 2008
Received in revised form 25 March 2009
Accepted 26 March 2009
Available online 8 May 2009

*Keywords:*
Fractal
Constructal
Void fraction
Microscale
Heat transfer
Two-phase

ABSTRACT

Two-phase air–water flows in a microscale fractal-like flow network were experimentally studied and results were compared to predictions from existing macroscale void fraction correlations and flow regime maps. Void fraction was assessed using (1) two-dimensional analysis of high-speed images (direct method) and (2) experimentally determined using gas velocities (indirect method). Fixed downstream-to-upstream length and width ratios of 1.4 and 0.71, respectively, characterize the five-level flow network. Channels were fabricated in a 38 mm diameter silicon disk, 250 μm deep disk with a terminal channel width of 100 μm. A Pyrex top allowed for flow visualization. Superficial air and water velocities through the various branch levels were varied from 0.007 m/s to 1.8 m/s and from 0.05 m/s to 0.42 m/s, respectively. Two-phase flow regime maps were generated for each level of the flow network and are well predicted by the Taitel and Dukler model. Void fraction assessed using the indirect method shows very good agreement with the homogeneous void fraction model for all branch levels for the given range of flow conditions. Void fraction determined directly varies considerably from that assessed indirectly, showing better agreement with the void fraction correlation of Zivi.



## 1. Introduction

During the past three decades, single-phase and two-phase heat transfer in microchannels has been actively studied. Depending upon the cooling loads required, the pressure drop across the flow channels can be significant. The benefit of latent energy accompanying two-phase heat transfer also has the drawback of flow instabilities. To mitigate the large drop in pressure, branching channel networks were proposed. However, the optimal design of the flow network depends significantly on the flow rate and size limitations as well as the heat transfer requirements. A one-dimensional single-phase model has been developed and integrated into a gradient-based optimization code that finds the flow network design that maximizes the benefit-to-cost ratio, defined as the energy removed by heat over the energy required to drive the fluid through the flow network. A similar one-dimensional model for predicting two-phase pressure drop has also been developed, but requires validation prior to implementation in an optimization code. Validation requires, which constitute the goals of the present study, (1) identifying flow regimes in these microscale branching flow networks to determine if all levels exhibit similar flow regimes or if the flow regimes change in different levels of the flow network, and (2) determining whether homogeneous or separated flow models best predict void fraction and pressure drop in two-phase flows in these branching flow networks. A logical first step is to conduct these experiments with gas–liquid flows.

## 2. Background

A single-phase laminar study was conducted by Tuckerman and Pease (1981), in which cooling capacities of up to 790 W/cm$^2$ were achieved. A number of single-phase investigations following this initial study reported a wide range of conclusions regarding the transition to turbulence as well as the applicability of macroscale correlations for microscale geometries. Based on a review of the existing literature, Obot (2000) and Sobhan and Garimella (2001) concluded that microscale flows are governed by the same principles as are conventional or macroscale flows and cited several potential reasons for observed variations in the experimental results.

Using a one-dimensional finite difference model and macroscale flow correlations for pressure drop and heat transfer, Pence (2000, 2002) predicted pressure drop and wall surface temperature for single-phase flows in fractal-like branching channel flow networks and heat sinks. Alharbi et al. (2003, 2004) validated this model using three-dimensional computational fluid dynamics and heat transfer, respectively. The validated model was subsequently used in optimization studies conducted by Enfield et al. (2005) and Heymann et al. (2008). The flow networks in these studies are fractal-like in nature, i.e., they have fixed downstream-to-upstream length and diameter/width scale ratios. In

* Corresponding author. Tel.: +1 541 737 7018; fax: +1 541 737 2600.
*E-mail addresses:* kwaky006@gmail.com (Y. Kwak), deborah.pence@oregonstate.edu (D. Pence), james.liburdy@oregonstate.edu (J. Liburdy), vinod.narayanan@oregonstate.edu (V. Narayanan).

0142-727X/$ - see front matter © 2009 Elsevier Inc. All rights reserved.
doi:10.1016/j.ijheatfluidflow.2009.03.014

**Nomenclature**

| | |
|---|---|
| $D_h$ | hydraulic diameter, $\frac{4WH}{2(W+H)}$ (μm) |
| $H$ | height of channel (μm) |
| $j$ | superficial velocity (m/s) |
| $k$ | branch level (–) |
| $L$ | length of channel (mm) |
| $\dot{m}$ | mass flow rate (kg/s) |
| $N$ | number of channels (–) |
| $p$ | white pixels in binarized image (–) |
| $q$ | pixels defining area of interest (–) |
| $R$ | number of frames in a movie (–) |
| $u$ | velocity (streamwise) (m/s) |
| $W$ | width of channel (μm) |
| $x$ | mass fraction (–) |

*Greek letters*

| | |
|---|---|
| $\alpha$ | void fraction (–) |
| $\beta$ | homogeneous void fraction (–) |
| $\lambda$ | wavelength (nm) |
| $\rho$ | density (kg/m$^3$) |

*Subscripts*

| | |
|---|---|
| $b$ | full bubble image |
| $c$ | bubble curvature image |
| $f$ | liquid phase |
| $g$ | gas phase or gas-based |
| *image* | image-based |
| $k$ | branch level index |
| $L$ | leading edge |
| $T$ | trailing edge |

contrast, application of constructal theory (Bejan, 1997) to disk shaped configurations resulted in non-fixed length scale ratios being deemed optimal (Wechsatol, 2002).

A two-phase heat transfer study was conducted by Bowers and Mudawar (1994), in which the benefits of minichannels and microchannels were compared to their drawbacks. For most conditions, the lower pressure drop through the minichannels was suggested to be preferable to the significantly higher pressure drop observed across the microchannels. The test devices in this study did not allow for flow visualization studies. A couple of the first successful studies in which flow regimes were identified include that of Jiang et al. (2001) in triangular microchannels with hydraulic diameters of approximately 25 and 50 μm and Hetsroni et al. (2001) in triangular microchannels having hydraulic diameters of 250 μm. The latter investigation included infrared temperature studies as well as high-speed imaging. Following a number of other two-phase flow investigations, several models for predicting heat transfer and pressure drop were developed. Representative examples include the two-regime elongated bubble model by Jacobi and Thome (2002) and an annular two-phase flow model by Qu and Mudawar (2003).

Zamfirescu and Bejan (2003) modeled two-phase frictional pressure drop in a constructal tree-shaped flow network. Daniels et al. (2005) included both the frictional and acceleration pressure loss contributions to predict two-phase boiling flow pressure drop in several fractal-like branching flow networks. In this latter study, a two-phase separated flow model was employed along with a variety of two-phase multiplier options for the frictional component and several void fraction correlations for predicting acceleration pressure drop. The same model was used by Daniels et al. (2007) to predict pressure drop in adiabatic two-phase cavitating flows, the results of which were experimentally validated by Daniels et al. (2008). The Zivi (1964) void fraction correlation and the two-phase multiplier proposed by Qu and Mudawar (2003) yielded the best agreement with experimentally measured pressure drops. Due to flow instabilities, one void fraction correlation was not clearly singled out over the others as best able to predict streamwise variations in void fractions.

Initial flow regime studies of gas–liquid flows through minichannels were performed by Triplett et al. (1999a). Channels ranged in diameter from 1.1 to 1.5 mm. A comparison of experimental flow regimes with the theoretical-based flow regime transition model by Taitel and Dukler (1976) showed relatively good agreement, except for the transition between slug and stratified flow. Chung and Kawaji (2004) studied nitrogen–water flows in circular tubes 50, 100, 250 and 530 μm in diameter and generated flow regime maps for each. Upon comparing their two-phase flow regime maps with the results of Triplett et al. (1999a), they found good agreement for the 250 and 530 μm diameter (mini)channels, but suggested a clear difference for the 50 and 100 μm diameter (micro)channels.

In Triplett et al. (1999b), experimental void fraction data were compared to a variety of homogeneous and separated flow correlations. Using these same correlations in a pressure drop model, experimental pressure drop was compared to models predictions. Both the experimental void fraction and the experimental pressure drop were best predicted for bubbly and slug flow regimes when the homogenous flow correlation was used. Using a mixture of air and water in circular tubes between 20 μm and 100 μm in diameter, Serizawa et al. (2002) found the experimental void

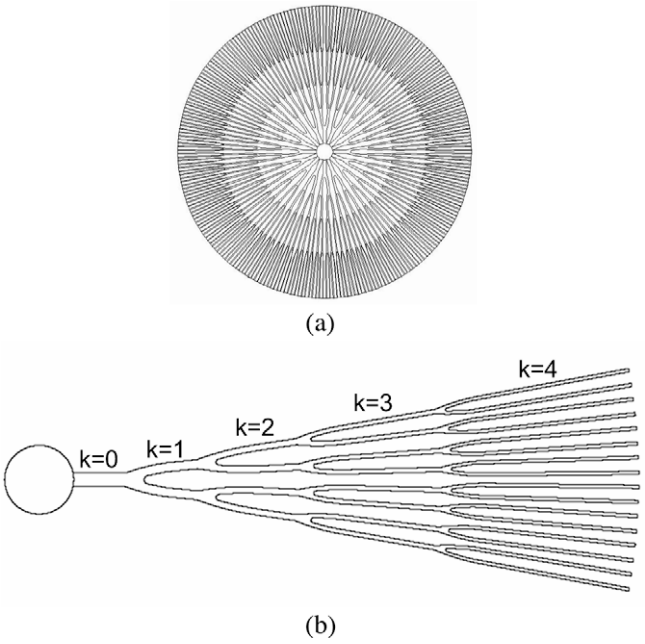


**Fig. 1.** (a) Test device schematic with a length scale ratio of 1.4 and (b) a single flow network with branch levels identified by *k*.

fraction was over predicted using the homogenous model, and recommended use of the correlation developed by Armand (1946), as reported in the translation by Beak (1959). Unsatisfied with the predictive capabilities of either the homogenous or Armand (1946) correlation, Chung et al. (2004) presented a new empirical void fraction correlation.

In the present study, a 38 mm diameter test device with a fractal-like branching channel network having five different channel levels and a fixed channel depth of 250 μm is used. A plan view schematic of the test device is provided in Fig. 1a, with a representative flow network, of which there are 16 in the test device, shown in Fig. 1b with labels denoting the branch level, $k$. Flow enters at the center of the disk through a 2 mm diameter inlet plenum and flows radially outward. The upstream-to-downstream width scale ratio and length scale ratio for this test device are fixed at

$$\frac{W_{k+1}}{W_k} = 2^{-1/2} \tag{1}$$

$$\frac{L_{k+1}}{L_k} = 2^{+1/2} \tag{2}$$

where the number two in Eqs. (1) and (2) represents the number of new downstream channels into which the upstream channel splits. The channel dimensions are provided in Table 1. Although the hydraulic diameter of a channel decreases with increasing level, $k$, there is an overall increase in flow area and a simultaneous decrease in both the superficial gas and liquid velocities. Given the changes in both superficial velocities and channel diameters as a function of branch level, the potential exists for changes in flow regime along the flow network for a fixed combination of inlet gas and liquid mass flow rates.

Flow regime maps for each level in the branching flow network are developed for three inlet mass flow rates of water and four inlet mass flow rates of air. These maps are compared to those of Taitel and Dukler (1976) and Chung and Kawaji (2004). Void fraction is assessed using two different techniques and plotted as a function of homogenous void fraction. These data are compared with the following void fraction correlations: Armand (1946), Zivi (1964), Chisholm (1973), and Chung et al. (2004).

## 3. Experimental facility

A manifold was designed to direct the two-phase mixture of air and water into the inlet of the test section and to collect and separate, through gravity, the two phases exiting the test section. The manifold is integrated in the flow loop, shown schematically in Fig. 2. The center column of the manifold is based on a vacuum chuck concept, which draws a vacuum between the test device and concentric o-ring seals. Details are also available in Kwak (2008).

Distilled deionized water is pumped from a reservoir using a Tuthill® 0.11ML/REV micro-gear pump with a maximum flow rate of 126 g/min at 690 kPa. The micro-gear pump is controlled with a DC power supply. The water flow rate is fine tuned with a needle valve located just downstream of the pump. If the water is seeded, as was the case for micro-PIV studies for liquid velocity measurements in Kwak (2008), it flows through a duct submerged in a Branson 2510DTH ultrasonic vibrator set at a power of 130 W and a frequency of 40 kHz. At the fastest flow rate used in the present study, this provided an 8-min residence time for the seeded flow in the vibration bath. The purpose of the ultrasonic vibrator is to disperse any agglomerated fluorescent particles evenly within the fluid. Just prior to the manifold inlet, air is injected into the water stream using a porous gas injector, shown schematically in Fig. 3, having an average pore size of 12 μm and average porosity of 15%. The gas injector design is similar to that reported in Xiong and Chung (2007).

**Table 1**
Channel dimensions.

| $k$ | $N_k$ | $H$ (μm) | $W$ (μm) | $L$ (mm) | $D_h$ (μm) |
|---|---|---|---|---|---|
| **0** | 16 | 250 | 400 | 1.6 | 308 |
| **1** | 32 | 250 | 283 | 2.3 | 265 |
| **2** | 64 | 250 | 200 | 3.2 | 222 |
| **3** | 128 | 250 | 141 | 4.5 | 180 |
| **4** | 256 | 250 | 100 | 6.4 | 143 |

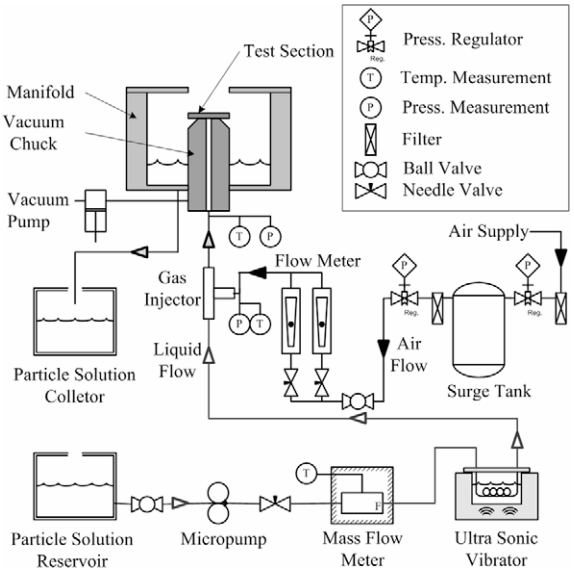


**Fig. 2.** Schematic diagram of flow loop.

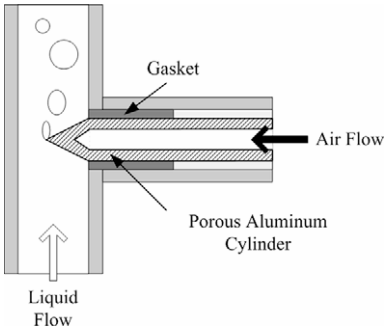


**Fig. 3.** Schematic diagram of gas injector.

The air, supplied by a compressor, is regulated on either side of a surge tank used to dampen pressure oscillations. The air is twice filtered, first with a 5 μm filter prior to the surge tank and with a second 1 μm filter located downstream of the surge tank. The flow of air is controlled by a needle valve.

Mass flow rates of both the air and water are necessary for determining the superficial flow rates needed to prepare flow regime maps. A Micromotion Coriolis mass flow meter, with a flow range of 0 to 1370 g/min and an accuracy of 0.10% of the flow rate, is used to measure the inlet water mass flow rate. Set to frequency mode, a "gate" is opened for five seconds and the frequency is measured and translated to a mass flow rate based on a manufacturer supplied calibration curve. This measurement was replicated 2000 times. One of two Gilmont® flowmeters are used to measure the volumetric flow rate of the air with an uncertainty of ±2% of the reading or one scale division. This measurement was replicated

14 times. To assess the mass flow rate of air requires an assessment of density immediately downstream of the volumetric flow meter. Therefore, the pressure and temperature of the air are measured by a Validyne® DP15 pressure transducer with an accuracy of 0.7 kPa and a T-type thermocouple with an accuracy of ±1 °C. Inlet temperature and pressure of the two-phase mixture are measured at the inlet of the manifold, which is approximately 7 cm below the inlet of the test device. The inlet temperature is measured with a Therm-X®, metal sheathed, 4-wire, resistance temperature detector (RTD) with an accuracy of 0.7 °C. The inlet pressure is measured with a Kulite Semiconductor® pressure transducer with a typical uncertainty in the voltage output of 0.1 mV. As the two-phase mixture discharged to the ambient conditions, both the barometric pressure and ambient temperature were also recorded using an Omega® PCL-1B absolute pressure transducer and an RTD with manufacturer uncertainties of ±0.35 kPa and ±0.3 °C, respectively. Pressure and temperature were recorded at 200 Hz for 5-s and replicated 2000 times.

Liquid velocity fields and interface velocities were determined under similar imaging conditions, i.e., using a laser light source, in Kwak (2008). For this reason, during acquisition of the interface velocities the water was seeded with 1.0 μm diameter fluorescent particles from Duke Scientific Co. The density of the fluorescent particles is 1.05 g/ml, compared with the 1 g/ml density of water at 20 °C. The excitation and emission wavelengths of the fluorescent particles are 542 nm and 612 nm, respectively. To intensify the liquid–gas interface for interface velocity measurements, Rhodamine B fluorescent dye with excitation and emission wavelengths of 526 nm and 580 nm, respectively, was added to the water at a molarity of $6 \times 10^{-8}$. Finally, to avoid particle agglomeration and prevent attachment of the seed particles to the channel walls during liquid velocity measurements, a 0.01% volume concentration of the surfactant, Triton X-100 was added to the seeded water.

To ensure consistent fluid properties for area-averaged void fraction and flow regime assessment, in which case illumination was achieved with a halogen light source, the water was prepared with the same Triton X-100 concentration. However, no seed particles were added, and a volume concentration of 0.08% of black food coloring was added to enhance visibility of the interface. Addition of the fluorescent Rhodamine B used in the micro-PIV studies for velocity assessment and the food dye used in the high-speed imaging studies for void assessment and regime identification do not significantly alter the fluid properties.

A high-speed–high-resolution (HSHR) Vision Research Phantom® V.5 camera was used to observe two-phase flow patterns and to assess two-dimensional area-averaged void fraction. In this configuration, light from a halogen source is introduced through a fiber optic cable and a series of optics, including a 0.63× video coupler, expander, diffuser, dichroic mirror and microscope objective lens, and then into the test device. The HSHR camera is controlled using a Dell® Inspiron 9200 laptop computer at an acquisition rate of 20 frames per second. A 10× and 20× objective were used for $k = 0$ through $k = 3$ levels and the $k = 4$ level, respectively, yielding a 2 μm per pixel and 1 μm per pixel resolution. A total of 2038 images were taken with the 10× objective having a $1024 \times 512$ pixel field of view and 4076 images with the 20× objective having a $1024 \times 256$ pixel field of view.

Micro-PIV was used to study liquid velocities and interface velocities (Kwak, 2008), the latter of which serves as the gas velocities for use in computing the void fraction indirectly. A double pulsed New Wave Solo PIV III-15 Nd:YAG laser with a major wavelength of 532 nm served as the light source for liquid velocity measurements. The laser light, at 19 mJ/s, was introduced normally into the test device through a series of optics, which for the micro-PIV measurements also included a high pass emission filter. The emitted filtered light passed into a Hisense MK2 12bit CCD camera with a $1344 \times 1024$ pixel resolution and a $6.45 \times 6.45$ μm per pixel pitch. The CCD camera and pulsed Nd:YAG laser were synchronized using a Dantec® system hub and controlled with Flow Manager® software.

For interface velocity measurements, 500 image pairs were acquired. The time interval between the two images within an image pair was varied with flow rates and branch levels to achieve a 100-pixel displacement of the interface. The 10x objective was used for all branch levels, with a few extra images taken in the $k = 3$ and $k = 4$ branch levels using the 20× objective. The 10× and 20× objectives have 14 μm and 5 μm depths of focus, respectively.

## 4. Data analysis

Using the theoretical model by Taitel and Dukler (1976), two-phase gas–liquid flow regimes at each level in the fractal-like branching channel network were generated as a function of superficial gas and liquid velocities. This mathematical model is based on physical phenomena to determine transition lines between the various flow regimes as a function of channel diameter, fluid properties, and orientation of the flow relative to gravity. Four flow regimes were considered in the model: stratified, intermittent, dispersed bubble and annular dispersed liquid, where intermittent flow includes slug, plug and elongated bubble flows.

These flow regime maps along with the homogeneous void fraction correlations were used to help develop the test plan shown in Table 2 to include several flow regimes for testing the predictive capabilities of the Taitel and Dukler (1976) model as well as provide a wide range of both measured and homogenous void fractions. Note that the superficial velocities in Table 2 are at the $k = 0$ branch level. The actual gas and liquid velocities suggest use of laminar friction factors in the Taitel and Dukler (1976) model for both air and liquid phases. However, final comparison of the experimental flow regimes with the flow regime maps suggested that use of the turbulent–turbulent coefficients provides a better match.

Flow regime maps are plotted as a function of liquid and gas superficial velocities. Superficial velocity of a phase is the velocity that would exist if the total flow rate of that phase passed through the total channel cross-sectional flow area. Assuming a fixed total mass flow rate through each of the branch levels, the superficial velocities through each branch, $k$, can be computed from

$$j_{g,k} = \frac{\dot{m}_g}{\rho_g N_k H_k W_k} \tag{3}$$

$$j_{f,k} = \frac{\dot{m}_f}{\rho_f N_k H_k W_k} \tag{4}$$

where

$$N_k = 16(2^k) \tag{5}$$

The coefficient 16 in Eq. (5) represents the number of branches at the $k = 0$ level. The mass flow rates in Eqs. (3) and (4) are those entering the manifold, hence the inlet plenum. Note that these superficial velocities will likely vary if the void fraction, hence the flow rate, are not uniformly distributed throughout each channel within a branch level.

The liquid mass flow rate was measured directly. The volume flow rate of gas was converted to mass flow rate using the density of air. Employing conservation of mass, the flow rate at the inlet of the test section was calculated. The inlet density was calculated using the ideal gas equation of state with a temperature of 25 °C and a pressure equal to one-half the pressure drop between the inlet of the manifold and ambient. This is a good approximation to the pressure at the inlet of the test device.

**Table 2**
Total flow rate test plan for regime identification and image-based void assessment. Gas velocity-based void fraction test plan are those cases shown in italicizes. Also provided are $j$ values at the $k = 0$ branch level, and β values and approximate $x$ values at every branch level.

| Water mass flow rate (g/min) [superficial liquid velocity (m/s)] | Air mass flow rate (g/min) [superficial air velocity (m/s)] | | | |
|---|---|---|---|---|
| | 8.2E−4 [0.007] | 1.6E−3 [0.014] | 1.1E−2 [0.104] | 2.1E−1 [1.80] |
| 40 [0.42] | Case 1<br>$x$ = 2E−5<br>($\beta$ = 0.02) | *Case 4*<br>*$x$ = 4E−5*<br>*($\beta$ = 0.03)* | Case 7<br>$x$ = 3E−4<br>($\beta$ = 0.20) | Case 10<br>$x$ = 5E−3<br>($\beta$ = 0.81) |
| 20 [0.21] | *Case 2*<br>*$x$ = 4E−5*<br>*($\beta$ = 0.03)* | *Case 5*<br>*$x$ = 8E−5*<br>*($\beta$ = 0.06)* | *Case 8*<br>*$x$ = 6E−4*<br>*($\beta$ = 0.33)* | Case 11<br>$x$ = 1E−2<br>($\beta$ = 0.90) |
| 5 [0.05] | Case 3<br>$x$ = 2E−4<br>($\beta$ = 0.12) | *Case 6*<br>*$x$ = 3E−4*<br>*($\beta$ = 0.21)* | Case 9<br>$x$ = 2E−3<br>($\beta$ = 0.67) | Case 12<br>$x$ = 4E−2<br>($\beta$ = 0.97) |

Void fraction correlations are assessed by plotting the void fraction, $\alpha$, as a function of homogenous void fraction, $\beta$, defined as

$$\beta = \frac{j_g}{j_g + j_f} \tag{6}$$

The void fraction correlations to which experiments are compared in this study include the homogenous flow correlation, in which $\alpha = \beta$, and the separated flow correlations of Armand (1946), Zivi (1964), Chisholm (1973) and Chung et al. (2004), which are, respectively,

$$\alpha = 0.833\beta \tag{7}$$

$$\alpha = \frac{1}{1 + \left(\frac{1-x}{x}\right)\left(\frac{\rho_g}{\rho_f}\right)^{2/3}} \tag{8}$$

$$\alpha = \left\{1 + \left[1 - x\left(1 - \frac{\rho_f}{\rho_g}\right)\right]^{1/2}\left(\frac{1-x}{x}\right)\left(\frac{\rho_g}{\rho_f}\right)\right\}^{-1} \tag{9}$$

$$\alpha = \frac{0.03\beta^{1/2}}{1 - 0.97\beta^{1/2}} \tag{10}$$

Air densities are computed as noted above and the density of water is assumed to be at standard conditions, which is 997 kg/m$^3$. The gas mass fraction, $x$, is computed from

$$x = \frac{\dot{m}_g}{\dot{m}_g + \dot{m}_f} \tag{11}$$

Experimental void fraction is measured *indirectly* from (Revellin et al., 2006)

$$\alpha_g = \frac{j_g}{u_g} \tag{12}$$

where $u_g$ is the average gas velocity determined from interface tracking. Both leading and trailing interface velocities were determined for a sufficient number of image pairs to yield a reliable average velocity, as was determined by assessing a running average. Use of this technique to assess void fraction is straightforward for gas–liquid flows, but requires a priori knowledge of the quality in boiling flows. As this will not be readily known as a function of downstream position for boiling flow studies in fractal-like flow networks, an alternate technique is desired.

Experimental void fraction, $\alpha_{image}$, is measured *directly* from two-dimensional images. The images are binarized such that the gas pixels are white whereas liquid pixels are black. Additional image process details are provided in Heymann et al. (2007) and Kwak (2008). In this analysis, gas is assumed to extend to the bottom of the channel. Although a reasonable assumption in channels with aspect ratios, $H_k/W_k$, less than unity (i.e., $k = 0$ and $k = 1$), this may not be the case for aspect ratios greater than unity. Therefore, this technique may over predict the volume-based void fraction in the deeper channels, i.e., $k > 2$, if the bubble does not fill the channel. If the method predicts different trends for high aspect ratio channels than for low aspect ratio channels, then a different methodology will be considered in future analyses, in which case, the bubble volume would be extrapolated into three-dimensions based on two-dimensional measured interface curvature.

In the present study, a simple correction to the two-dimensional void fraction is proposed. As observed in Fig. 4a, there is a dark region surrounding the region of gas. This is attributed to the curved interface, as discussed in Kwak (2008). The void defined by the outer edge of the interface curvature is shown in Fig. 4b. Isolating the curved interface shown in Fig. 4c from the full void region in Fig. 4b is achieved by varying the binarization threshold during image processing. The correction is achieved by subtracting half of the interface area in Fig. 4c from the area of the void in Fig. 4b. The equation for computing image-based void fraction is

$$\alpha_{image} = \frac{\sum_{j=1}^{r}\sum_{i=1}^{q}(p_b - 0.5p_c)}{rq} \tag{13}$$

where $p$ represents a white pixel in a binarized image, $r$ is the number of frames in a movie, and $q$ represents the number of pixels defining the area of interest in which the image-based void fraction, $\alpha_{image}$, is being assessed. Subscripts $b$ and $c$ represent the bubble (void) and curvature, respectively. The region of interest is shown in Fig. 4d.

## 5. Results and discussion

Flow pattern observations at each branch level are characterized and then compared with flow regime maps from Taitel and Dukler (1976) and Chung and Kawaji (2004). Experimental void fraction results, based on gas velocities and area-averaged

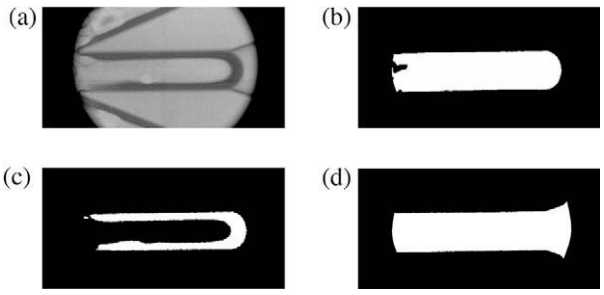


**Fig. 4.** (a) Raw HSHR image of bubble, (b) bubble, (c) curved liquid/vapor interface, and (d) region of interest for void fraction assessment.

| Liquid flow rate (superficial liquid velocities) | Gas flow rate (superficial gas velocities) | | | |
|---|---|---|---|---|
| | **$8.2\times10^{-4}$ g/min (0.007 m/s)** | **$1.6\times10^{-3}$ g/min (0.014 m/s)** | **$1.2\times10^{-2}$ g/min (0.104 m/s)** | **$2.1\times10^{-1}$ g/min (1.80 m/s)** |
| **40 g/min (0.42 m/s)** | *Case 1* bubbly/slug  | *Case 4* bubbly/slug  | *Case 7* bubbly/slug  | *Case 10* slug/ring 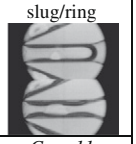 |
| **20 g/min (0.21 m/s)** | *Case 2* bubbly/slug  | *Case 5* bubbly/slug  | *Case 8* bubbly/slug  | *Case 11* slug/ring 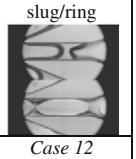 |
| **5 g/min (0.05 m/s)** | *Case 3* slug  | *Case 6* slug  | *Case 9* slug  | *Case 12* ring/annular 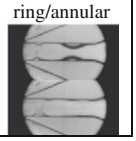 |

**Fig. 5.** Flow patterns variations with gas and liquid flow rates in the $k = 0$ branch level.

| Branch level | Case 1 | Case 6 |
|---|---|---|
| **k=0** | bubbly/slug 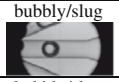 | slug 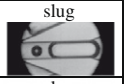 |
| **k=1** | bubbly/slug 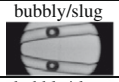 | slug  |
| **k=2** | bubbly/slug  | slug  |
| **k=3** | slug  | slug  |
| **k=4** | slug  | slug 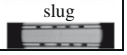 |

**Fig. 6.** Flow pattern variations with branch level for case 1 and case 6.

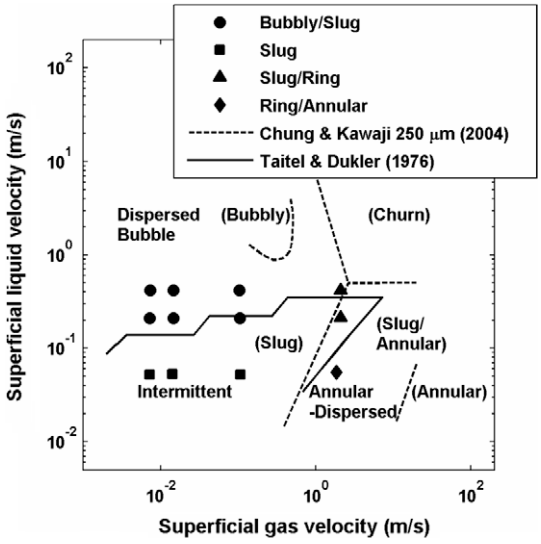


**Fig. 7.** Flow regime map for $k = 0$ branch level and 12 test cases.

two-phase images, are compared with existing void fraction correlations.

### 5.1. Flow regimes

The void classification scheme used in the present study includes bubbly, slug, ring and annular flow. Bubbly flow is defined as the presence of one or more voids each having a diameter equal to or smaller than the channel width. Slug flow is defined when the void length is larger than the width of channel, but short enough not to occupy the entire region of interest. The ring flow pattern represents a void filling an entire channel length (i.e., the flow field) with a very thick liquid film. This thick liquid film has a symmetrical wave pattern about the centerline of the channel. Finally, annular flow patterns are defined when an irregular, very thin liquid film occurs around a gas core and the void extends the entire length of the field of view.

Fig. 5 shows two-phase flow patterns in the $k = 0$ level and over the range of gas and liquid mass flow rates corresponding to the test plan reported in Table 2. Reported along the top row are gas mass flow rates and superficial gas velocities, with liquid mass flow rates and superficial liquid velocities reported in the first column. For the higher superficial liquid velocities of 0.21 m/s and 0.42 m/s and the superficial air velocities between 0.007 m/s and 0.104 m/s, bubbly and slug flow patterns are observed. These velocity combinations correspond with test cases 1, 2, 4, 5, 7 and 8. When the superficial liquid velocities are reduced for these same superficial gas velocities, slug flow patterns are observed, as in the experimental test cases of 3, 6 and 9. Case 10 and case 11 show mixed gas–liquid patterns of slug and ring flows, which occur with an increase in superficial gas velocity while holding the superficial liquid velocities constant. The experimental test case 12 shows both ring (top) and annular flow (bottom) patterns. Cases exhibiting multiple flow regime patterns are considered to be in the transitional region between the identified regimes.

Fig. 6 shows the two-phase flow pattern for cases 1 and 6 at all branch levels. In case 6, flow starts out in the $k = 0$ branch as slug flow and continues to exhibit slug flow downstream. Although the hydraulic diameter decreases with increasing branch level, $k$, the nature of the bifurcating flow network is an increase in flow area;

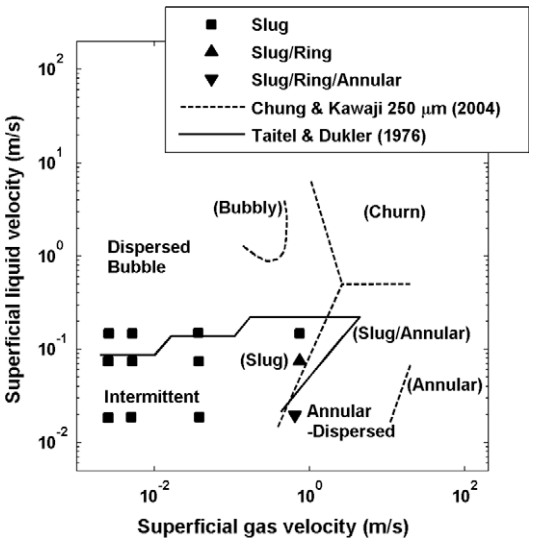


**Fig. 8.** Flow regime map for $k = 3$ branch level and 12 test cases.

hence, the superficial velocities decrease with increasing $k$. Case 1 shows both bubbly and slug flow at the $k = 0$ and $k = 1$ branch levels and slug flow further downstream. The cases exhibiting bubbly-slug flow in Fig. 5 transition to slug flow in the $k = 2$ and $k = 3$ levels, respectively, for liquid mass flow rates of 20 and 40 g/min. Typical uncertainties in liquid and gas mass flow rates are ±0.1 g/min and ±4%, respectively, whereas uncertainties in the superficial liquid and gas velocities are ±0.0001 m/s and ±5%, respectively.

It should be mentioned that no backflow, routinely observed for non-throttled two-phase convective boiling flows, was observed for this gas-injected flow. However, obvious from Fig. 5 cases 1, 6, and 9 and several images in Fig. 6, the void fraction is not always identical in each channel within a branch level.

### 5.2. Flow regime map comparison

Two-phase, gas–liquid, flow pattern observations made in a fractal-like branching channel network are compared to flow regime maps in Chung and Kawaji (2004) for a 250 μm diameter tube and from the theoretical model of Taitel and Dukler (1976) using the properties of water and air and a hydraulic diameter of 308 μm. Flow regime maps are plotted as a function of superficial gas and superficial liquid velocities on logarithmic axes. Fig. 7 shows a flow regime map with two-phase flow patterns for all 12 test cases at the $k = 0$ branch level. Regimes for the present study are identified by symbols defined in the legend. The transition lines representing the Chung and Kawaji (2004) experimental flow regime map are displayed as dashed lines, with flow regimes identified by enclosed parentheses. Taitel and Dukler (1976) flow regime maps are presented as solid lines. In Fig. 7, Taitel and Dukler (1976) flow regimes are identified as dispersed bubble, intermittent and annular-dispersed flows, which can also be expressed as bubbly, slug and annular flows, respectively. The latter terminology is that used in the present study. A similar map is plotted in Fig. 8 for the $k = 3$ branch, which has a hydraulic diameter of 180 μm.

Evident from both Figs. 7 and 8 is that the Taitel and Dukler (1976) flow regime maps show good agreement with the flow pattern observations in the $k = 0$ and $k = 3$ branch levels of the fractal-like branching channel network. The Chung and Kawaji (2004) map shows better agreement with experimental data than does the Taitel and Dukler (1976) model at the transitions between slug and ring and between slug and annular flow, although the Taitel and Dukler (1976) predictions are not at all bad. It should be noted that the fluid properties employed in the model were that of pure water.

### 5.3. Gas velocities

Time-averaged interface velocities were assessed. As was done in Heymann et al. (2007) three different types of void images were analyzed. These include cases in which (1) a leading edge only is, (2) a trailing edge only is, and (3) both leading and trailing edges are detected in the field of view in both images. These cases are consistent with a void entering the region of interest, leaving the region of interest, and completely within the region of interest, respectively. Interface velocities determined from image pairs with both leading and trailing edge voids in the $k = 0$ level are plotted in Fig. 9. The average of leading and trailing velocities are essentially identical, 0.24 m/s with a standard deviation of ±0.05 m/s. The high degree of scatter is attributed to temporally varying flow rate at the location in which the images were acquired. Average leading only and trailing only velocity assessments were 0.23 m/s with similar standard deviations. The typical average uncertainty in the measured interface velocities is 0.0075 m/s, or approximately ±3%.

### 5.4. Void fraction comparison with correlations

Fig. 10 shows void fractions computed from the gas velocity, $\alpha_g$, and void fractions determined from two-dimensional images,

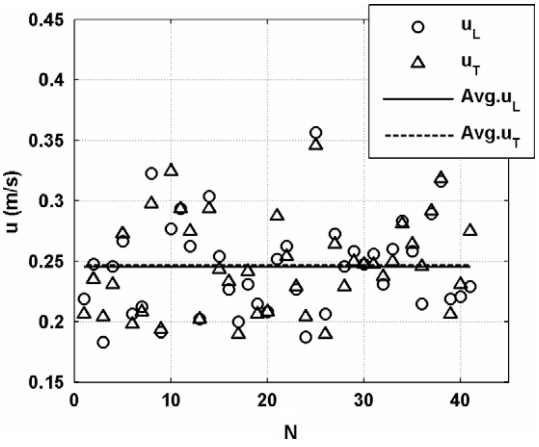


**Fig. 9.** Interface velocities.

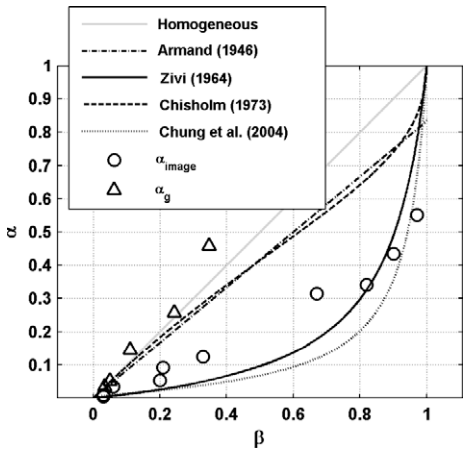


**Fig. 10.** Void fraction in $k = 0$ branch level and 12 cases for image-based void and five cases for gas velocity-based void.

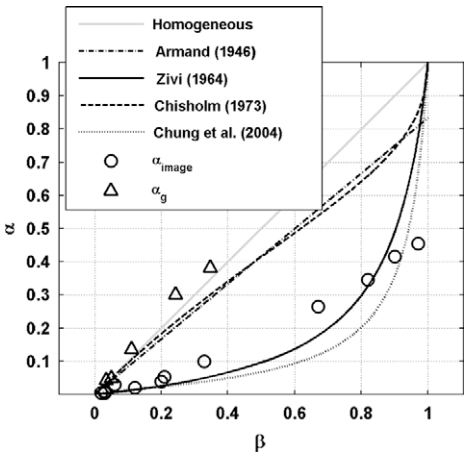


**Fig. 11.** Void fraction in $k = 3$ branch level and 12 cases for image-based void and five cases for gas velocity-based void.

$\alpha_{image}$, plotted as a function of homogenous void fraction, $\beta$, for the $k = 0$ branch level. Triangles represent the experimental void fraction resulting from gas velocity data, and circles represent experimental void fraction based on area-averaged images. Also, shown in Fig. 10 are void fraction predictions assuming homogenous flow and predictions from the separated flow correlations of Armand (1946), Zivi (1964), Chisholm (1973) and Chung et al. (2004). The experimental void fraction determined using the gas velocity, $\alpha_g$, follows most closely the homogeneous flow trend, a result also observed by Revellin et al. (2006). However, the experimental void fraction determined using the area-averaged images, $\alpha_{image}$, has a noticeably different trend from that of $\alpha_g$. Rather, the image-based void fractions are somewhat under predicted by both the Zivi (1964) and Chung et al. (2004) void fraction correlations between the homogeneous void fraction values of 0.1 and 0.7, with the Zivi (1964) correlation yielding better predictions. It should be noted that the correlation by Chung et al. (2004) is based on direct image data averaged over space and time, similar to the image method reported in this study. The Zivi (1964) correlation is based on kinetic energy theory.

Typical uncertainties in the homogeneous void fraction and in the measured void fractions (for both the direct and indirect techniques) are ±4 and ±5%, respectively. Values of $\alpha_g$ greater than the homogenous void fraction, as is observed in Fig. 10, implies that the liquid is moving, on average, faster than the gas. These observations are believed to be a result of spatial flow maldistribution, i.e., the time-averaged flow through one flow network defined by one $k = 0$ branch level may be different than that through a different $k = 0$ branch level.

Similar observations to those observed for the $k = 0$ branch level are made in the $k = 0$ branch level, as noted in Fig. 11. However, the Zivi (1964) correlation tends to predict the experimental values of $\alpha_{image}$ in this smaller diameter channel better than in the larger $k = 0$ channel. As was generally observed, the $\alpha_{image}$ data were better predicted by the Zivi (1964) correlation in the 0.1 to 0.7 range of $\beta$ as the channel diameter decreased, which corresponds with increases in level $k$. For the range of test conditions considered in the present investigation, the assumption that bubbles are as deep as the channel appears to be valid for image-based assessment of void fraction.

As a final note, void fractions computed using gas velocities are based on the assumption that no liquid film surrounds the bubble. As the image-based data show, a film does exist, which explains the overestimation of $\alpha_g$ compared with $\alpha_{image}$. In summary, the use of the Zivi (1964) correlation is recommended for use in two-phase predictive models for branching flow networks.

## 6. Conclusions

In summary, the Taitel and Dukler (1976) model fairly well predicts flow regimes in the various branch levels in the fractal-like flow network given the flow rate ranges in the present study. The map generated by Chung and Kawaji (2004) for a hydraulic diameter of 250 μm also tends to predict the observed flow regimes fairly well.

The experimental void fractions based on gas velocity are best predicted by the homogeneous flow model, as was the case in Revellin et al. (2006). On the other hand, the image-based void fraction data in the present study agree better with those correlations based on image processing and on kinetic energy theory, as reported in Chung et al. (2004) and Zivi (1964), respectively. Because void fractions determined indirectly from gas velocity assume no liquid film, it is concluded that experimental data measured directly from two-phase flow images is more reliable. These data are most accurately modeled using the Zivi (1964) model.

The closest study performed to date in a similar fractal-like flow network is that of Daniels et al. (2008) for adiabatic flow boiling, i.e., for vapor–liquid flows. The void fraction correlation in the pressure drop model that best predicted experimental pressure drop results was that of Zivi (1964), which follows trends of the image-based data. The two-phase multiplier used was also found to influence the results. Direct comparison between the present study and that of Daniels et al. (2008) is not possible due to differences in length scale ratios, which is 1.4 for the present study and 0.71 in Daniels et al. (2008), and in the type and rates of flow of the two phases.

## Acknowledgements

The author would like to thank the Office of Naval Research for support under contract number N00014-06-1-0017, Dr. Mark Spector, program manager. Also, the authors are grateful to Mr. Douglas Heymann for his tireless dedication to the image processing part of this research effort.

## References

Alharbi, A.Y., Pence, D.V., Cullion, R.N., 2003. Fluid flow through microscale fractal-like branching channel networks. Journal of Fluids Engineering 125 (6), 1051–1057.

Alharbi, A.Y., Pence, D.V., Cullion, R.N., 2004. thermal characteristics in micro-scale fractal-like branching channels. Journal of Heat Transfer 126 (5), 744–752.

Armand, A.A., 1946. The resistance during the movement of a two-phase system in horizontal pipes. Izvestiya Vsesoyuznogo Teplotekhnicheskogo Instituta 1, 16–23 (in Russian, see translation by V. Beak in 1959).

Beak, V., 1959. The resistance during the movement of a two-phase system in horizontal pipes. Atomic Energy Research Establishment Transactions, 828.

Bejan, A., 1997. Constructal tree network for fluid flow between a finite-size volume and one source or sink. Revue Generale de Thermique 36 (8), 592–604.

Bowers, M.B., Mudawar, I., 1994. High flux boiling in low flow rate, low pressure drop mini-channel and micro-channel heat sinks. International Journal of Heat and Mass Transfer 37 (2), 321–332.

Chisholm, D., 1973. Void fraction during two-phase flow. Journal Mechanical Engineering Science 13 (3), 235–236.

Chung, P.M.Y., Kawaji, M., 2004. The effect of channel diameter on adiabatic two-phase flow characteristics in microchannels. International Journal of Multiphase Flow 30, 735–761.

Chung, P.M.Y., Kawaji, M., Kawahara, A., Shibata, Y., 2004. Two-phase flow through square and circular microchannels – effects of channel geometry. Journal of Fluids Engineering 126, 546–552.

Daniels, B.J., Pence, D.V., Liburdy, J.A., 2005. Predictions of flow boiling in fractal-like branching microchannels, in: Proceedings of the ASME International Mechanical Engineering Conference and Exposition, FED-261, Orlando, FL, pp. 359–368.

Daniels, B.J., Liburdy, J.A., Pence, D.V., 2007. Adiabatic flow boiling in fractal-like microchannels. Heat Transfer Engineering 28 (10), 817–825.

Daniels, B.J., Liburdy, J.A., Pence, D.V., 2008. Experimental studies of adiabatic flow boiling in fractal-like branching micro-channels. In: Proceedings of the ASME International Mechanical Engineering Congress and Exposition, Boston, MA, IMECE2008-69240.

Enfield, K., Pence, D.V., Narayanan, V., 2005. Optimization of single-phase microscale fractal-like branching flow heat sinks. In: Proceedings of the Engineering Conference International Heat Transfer and Fluid Flow in Microscale II, Castelvecchio Pascoli, Italy.

Hetsroni, G., Mosyak, A., Segal, Z., 2001. Two-phase flow in microchannels. In: Proceedings of the ASME Fluid-Physics and Heat Transfer for Macro- and Micro-Scale Gas–Liquid and Phase-Change Flows, vol. HTD-369, no. 3, pp. 87–93.

Heymann, D., Kwak, Y., Edward, L., Liburdy, J., Narayanan, V., Pence, D., 2007. Area-averaged void fraction analysis of flow boiling in a microscale branching channel network. In: Proceedings of ASME – Pacific Rim Technical Conference on Integration and Packaging of MEMS, NEMS, and Electronic Systems, IPACK2007-33517.

Heymann, D., Enfield, K., Pence, D., Narayanan, V., 2008. Gradient-based optimization of single-phase microscale fractal-like branching channel heat sinks. In: Proceedings of the Engineering Conference International Heat Transfer and Fluid Flow in Microscale III, Whistler, BC, Canada.

Jacobi, A.M., Thome, J.R., 2002. Heat transfer model for evaporation of elongated bubble flows in microchannels. Journal of Heat Transfer 124 (6), 1131–1136.

Jiang, L., Wong, M., Zohar, Y., 2001. Forced convection boiling in a microchannel heat sink. Journal of Microelectromechanical Systems 10 (1), 80–87.

Kwak, Y., 2008. Experimental Study of Two-Phase Gas–Liquid Flow in a Microscale Fractal-Like Branching Flow Network, Ph.D. Thesis, Oregon State University, Corvallis, OR.

Obot, N.T., 2000. Toward a better understanding of friction and heat/mass transfer in microchannels – a literature review. In: Celata, G.P. (Ed.), Proceedings of the Engineering Conference International Heat Transfer and Transport Phenomena in Microscale. Begell House, New York, pp. 72–79.

Pence, D.V., 2000. Improved thermal efficiency and temperature uniformity using fractal-like branching channel networks. In: Celata, C.P. (Ed.), Proceedings of the Engineering Conference International Heat Transfer and Transport Phenomena in Microscale. Begell House, New York, pp. 142–148.

Pence, D.V., 2002. Reduced pumping power and wall temperature in microchannel heat sink with fractal-like branching channel networks. Microscale Thermophysical Engineering 6 (4), 319–330.

Qu, W., Mudawar, I., 2003. Flow boiling heat transfer in two-phase micro-channel heat sinks – II. Annular two-phase flow model. International Journal of Heat and Mass Transfer 46 (15), 2755–2771.

Revellin, R., Vincent, D., Ursenbacher, T., Thome, J.R., Zun, I., 2006. Characterization of diabatic two-phase flows in microchannels: flow parameter results for R-134a in A 0.5 mm channel. International Journal of Multiphase Flow 32 (7), 755–777.

Serizawa, A., Feng, Z., Kawara, Z., 2002. Two-phase flow in microchannels. Experimental Thermal and Fluid Science 26 (6–7), 703–714.

Sobhan, C.B., Garimella, S.V., 2001. A comparative analysis of studies on heat transfer and fluid flow in microchannels. Microscale Thermophysical Engineering 5 (4), 293–311.

Taitel, Y., Dukler, A.E., 1976. A model for predicting flow regime transitions in horizontal and near horizontal gas–liquid flow. AIChE Journal 22 (1), 47–55.

Triplett, K.A., Ghiaasiaan, S.M., Abdel-Khalik, S.I., Sadowski, D.L., 1999a. Gas–liquid two-phase flow in microchannels. Part I: two-phase flow patterns. International Journal of Multiphase Flow 25 (3), 377–394.

Triplett, K.A., Ghiaasiaan, S.M., Abdel-Khalik, S.I., LeMouel, A., McCord, B.N., 1999b. Gas–liquid two-phase flow in microchannels. Part II: void fraction and pressure drop. International Journal of Multiphase Flow 25 (3), 395–410.

Tuckerman, D.B., Pease, R.F.W., 1981. High-performance heat sinking for VLSI. IEEE Electron Device Letters EDL-2 (5), 126–129.

Wechsatol, W., Lorente, S., Bejan, A., 2002. Optimal tree-shaped networks for fluid flow in a disc-shaped body. International Journal of Heat and Mass Transfer 45 (25), 4911–4924.

Xiong, R., Chung, J.N., 2007. An experimental study of the size effect on adiabatic gas–liquid two-phase flow patterns and void fraction in microchannels. Physics of Fluids 19 (9), 0333011–0333018.

Zamfirescu, C., Bejan, A., 2003. Constructal tree-shaped two-phase flow for cooling a surface. International Journal of Heat and Mass Transfer 46, 2785–2797.

Zivi, S.M., 1964. Estimation of steady-state steam void-fraction by means of the principle of minimum entropy production. Journal of Heat Transfer 86, 247–252.